Circulating Current and ZVS-on of a Dual Active Bridge DC-DC Converter: A Review

SHUAI SHAO[1], (Member, IEEE), **HUI CHEN**[2], **XINKE WU**[1], (Member, IEEE), **JUNMING ZHANG**[1], (Senior Member, IEEE), AND **KUANG SHENG**[1], (Senior Member, IEEE)

[1]College of Electrical Engineering, Zhejiang University, Hangzhou 310027, China
[2]School of Information and Electrical Engineering, Zhejiang University City College, Hangzhou 310015, China

Corresponding author: Hui Chen (chenh@zucc.edu.cn)

ABSTRACT Dual active bridge (DAB) dc–dc converters have several attractive features including auto-adjust bidirectional power flow, wide voltage gain range, and zero voltage switching (ZVS)-on capability. Various applications based on DAB including solid-state transformer in power grids and traction, energy storage system, and electric vehicle on-board chargers have been proposed by academics. Nevertheless, industrial applications based on DABs are still seldom mainly due to the circulating current and loss of ZVS problems under certain load and voltage gain conditions. There is an intensive research effort underway to solve these problems recently. This paper presents the state-of-the-art view in the cause of circulating current and loss of ZVS and surveys the solutions to these problems.

INDEX TERMS Circulating current, dc-dc converter, dual active bridge, reactive power, ZVS-on.

I. INTRODUCTION

The last decade has seen explosive growth in renewable energy including wind, solar, biomass, tidal, geothermal etc. Led by wind and solar power, renewable energy accounted for almost a third of the increase in primary energy in 2016 [1]. The renewable energy is distributed and intermittent by nature, and the existing power system infrastructure cannot cope with its high penetration. To overcome these problems, a series of technologies including energy storage systems (ESSs) and micro-grids are introduced. ESSs such as batteries, super-capacitors and flywheels can compensate the fluctuations and maintain a smooth and continuous power flow. A micro-grid can be regarded as a controlled cell within the power system that can be operated as a single aggregated load or source. Different levels of micro-grids are hierarchically interconnected and formed the future ''smart grid'' [2]–[4]. Micro-grid/smart-grid is a promising solution to transform the distribution grids from conventional central energy production and unidirectional flow, to de-central energy production and bidirectional flow [2], [5].

In both ESSs and micro-grids, isolated bidirectional dc-dc (IBDC) converters are usually required. For ESSs such

The associate editor coordinating the review of this manuscript and approving it for publication was Ahmad Elkhateb.
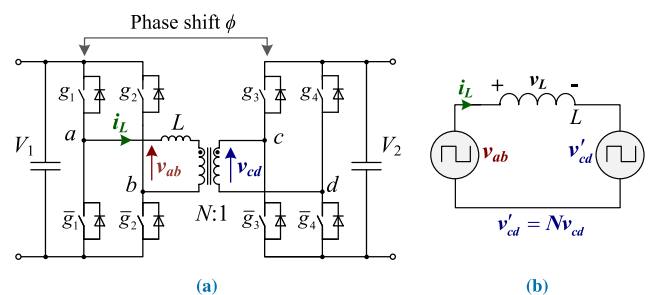

FIGURE 1. Topology of a DAB converter (a) and its equivalent circuit (b).

as batteries and super capacitors, an IBDC is utilized as an interface to allow energy exchange between ESSs and the rest of the system. For micro-grids, IBDCs are stacked and operate as the so-called solid state transformer (SST), to manage the power flow between micro-grids and the upstream distribution grid [6]. In these applications, the transformer in an IBDC provides necessary galvanic isolation and/or voltage matching.

Various IBDC topologies have been proposed, including bidirectional resonant converters, dual flyback, dual-Cuk, dual-push-pull, dual active bridge (DAB) [7]. For the ESSs and micro-grids applications, the DAB (Fig. 1) proposed by

Doncker *et al.* [8], [9] is one of the most promising topologies for the following reasons:

- Auto-adjust bidirectional power flow, ideal for SSTs and ESSs in micro-grids that requires fast power flow direction transition.
- Wide voltage conversion gain range, excellent to interface ESSs such as batteries or super-capacitors, whose voltage can vary significantly under different states of charge.
- Zero voltage switching (ZVS) capability, able to achieve high efficiency with proper control.

Various applications employing DABs have been proposed. SSTs based on DABs in power grids have been introduced to interconnect different scale micro-grids [6], [10], [11] or to connect different level of dc grids [12]–[17]. Power electronic traction transformer (PETT) using DABs can reduce the weight, add additional functionalities and improve energy efficiency compared to on-board line frequency transformer [18]–[21]. DAB is also a promising solution for on-board battery chargers in plug-in electric vehicle (PEV), especially when the vehicle-to-grid (V2G) function is required [22]–[25]. With wide bandgap devices and sinusoidal charging [22], high power density (3.3kW/L) and high efficiency (> 97%) [25] can be achieved. Other applications including ESS interface converters [26], [27], airborne wind turbine [28], uninterrupted power supply (UPS) [29], and power load emulator [30] have also been reported.

Most of these applications, however, are constrained in the academia, there are still seldom products found in industry. The primary reasons are the large circulating current and loss of ZVS under unmatched gain and light load conditions, which can significantly decrease the efficiency. The circulating current, similar to the reactive current in power system, does not transfer any energy, but increases power device conduction losses and transformer copper losses. The loss of ZVS-on, on the other hand, will significantly increase the switching losses, especially under high frequency applications. There is an intensive research effort underway to solve these problems recently. This paper comprehensively explains the reasons of circulating current and loss of ZVS-on, and reviews the recent solutions to these problems. Compared to the existing reviews [7], [31], this paper provides a more in-depth analysis and recent progress for DAB on circulating current suppression and ZVS-on.

II. CIRCULATING CURRENT SUPPRESSION

As shown in Fig. 1, a DAB consists of two H-bridges located on the primary and secondary sides of a transformer. The transformer provides the isolation and voltage matching between the low- and high- voltage buses. The transformer leakage inductance (or plus an additional inductor) serves as the instantaneous energy storage element [32]. A DAB can be simplified as Fig. 1 (b) assuming ideal power semiconductor devices and transformer.

The output voltage and power of a DAB are normally regulated by shifting phases of the square voltage generated
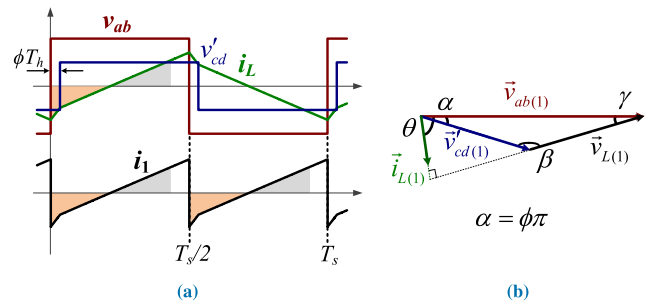

FIGURE 2. A DAB modulated using SPS: (a) key waveforms, (b) fundamental phasor diagram.

by H-bridges (v_{ab} and v_{cd} in Fig. 1). The simplest modulation principle is illustrated in Fig. 2 (a), in which v_{ab} and v_{cd} are with constant 50% duty cycle and only their phase difference is manipulated to regulate the output voltage [9]. This modulation method is termed as the single phase shift (SPS) [33].

When a DAB modulated using SPS, the inductor current i_L involves a portion of reverse current (orange shaded area in Fig. 2 (a)) that transmits power backwards, and i_L has to increase its forwarding part (gray shaded area) to maintain the certain transmitted power. The orange and gray shaded portion currents are called circulating current (or reactive current) in a DAB. Similar to the reactive current in an ac grid, the circulating current does not transfer any energy, but produces power device conduction losses and transformer copper losses.

The amount of circulating current is closely related to voltage gain M, which is defined as $M = NV_2/V_1$. To explain this phenomenon, the phasor diagram Fig. 2 (b) is employed, where the phasors $\vec{v}_{ab(1)}, \vec{v}'_{cd(1)}, \vec{i}_{L(1)}, \vec{v}_{L(1)}$ represent fundamental components of the voltages and current in Fig. 1 (b). These phasors satisfy:

$$\begin{cases} \vec{v}_{L(1)} = \vec{v}_{ab(1)} - \vec{v}'_{cd(1)} \\ \vec{i}_{L(1)} = \vec{v}_{L(1)}/j\omega L \end{cases} \qquad (1)$$

The angles between these phasors satisfy the law of sines:

$$\begin{cases} \beta + \gamma = \pi - \alpha \\ \dfrac{\sin \gamma}{\sin \beta} = \dfrac{|\vec{v}'_{cd(1)}|}{|\vec{v}_{ab(1)}|} = M \\ \theta = \dfrac{\pi}{2} - \gamma \end{cases} \qquad (2)$$

For a given α ($\alpha = \phi\pi$), a small M leads to a small γ and a large θ according to (2) and Fig. 2 (b) when $M < 1$. A large θ (the angle between $\vec{v}_{ab(1)}$ and $\vec{i}_{L(1)}$), results a high percentage of the reactive power. The circulating current will increase further as M decreases.

Various methods have been proposed to suppress the circulating current and to improve the DAB efficiency. These methods can be categorized into two types, hardware methods and duty cycle methods.
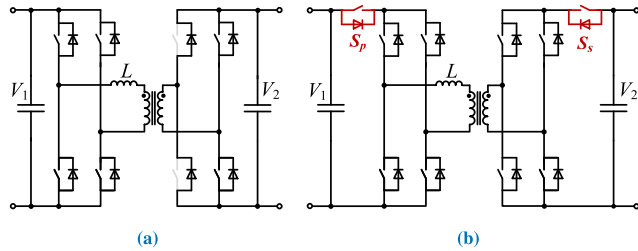
FIGURE 3. Typical circuits to suppress the circuiting current using unidirectional diodes [34]–[36].
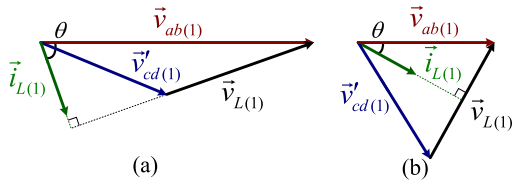

FIGURE 4. Fundamental phasor diagrams with the same output power: (a) $M = 0.5$, (b) $M = 1$.

A. HARDWARE METHODS

Replacing the bidirectional power switching devices with unidirectional diodes can suppress the circulating current as shown in Fig. 3, where the power transfers from left to right side. Simply turning off the power switches in one of the secondary legs, as shown in Fig. 3 (a), can block the circulating current on the secondary side [34], [35]. Fig. 3(b) shows a method that can suppress the circulating current on both primary and secondary sides, where additional power switching devices S_p, S_s can be added [36]. These two methods are straightforward, however, the automatic bidirectional power flow capability is sacrificed and maximum transferred power of these circuits are also smaller than that of a normal DAB. In addition, in the method shown in Fig. 3(b), there are additional conduction and switching losses, and careful modulation is required to give freewheeling paths for the inductor current.

Varying the circuit between full- and half- bridges (termed as hybrid bridge) to let the actual voltage gain around unity can also reduce the circulating current. Fig. 4 illustrates the working principle using fundamental components phasors of the i_L, v_{ab} and v_{cd}. The output powers of Fig. 4 (a) and (b) are the same, but the voltage gains M are 0.5 and 1 respectively. With larger θ and $|\vec{v}_{ab}|$, the circulating current of Fig. 4 (a) is much larger than that of Fig. 4 (b). The change from Fig. 4 (a) to (b) can be realized by varying the primary circuit from full- to half- bridge. Fig. 5 presents typical methods to implement DAB circuits with hybrid bridges.

By adding two blocking capacitors (C_{bp}, C_{bs}), the circuits in Fig. 5 (a) on both primary and secondary sides can operate as full- or half- bridges depending on the voltage gain M [37]. For instance, when $M = NV_2/V_1 = 0.5$, switching S_2 off and $\bar{S}_2$ on, the primary side circuit becomes a half bridge, and C_{bp} blocks the dc-offset. However, this method is only effective at certain gain conditions (M is around 0.5, 1, or 2).
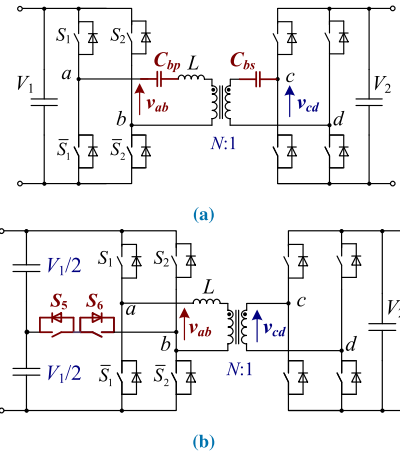

FIGURE 5. Varying the circuit between full- and half- bridges: (a) using blocking capacitors [37], (b) using two auxiliary power switches [38].
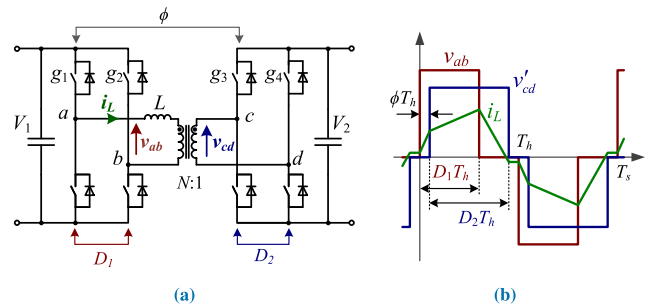

FIGURE 6. Phase shift ratios definitions on the circuit (a) and on the key waveforms (b).

The hybrid bridge can also be realized by adding two auxiliary power switches as shown in Fig. 5 (b) [38]. The primary circuit operates as a full-bridge when S_5, S_6 are off, and as a half-bridge when S_5, S_6 are on and S_2, $\bar{S}_2$ are off. The two auxiliary switches adds another degree of freedom to the DAB, actually, by coordinating the switching of S_1, S_2 and S_5, S_6, v_{ab} can output a four level voltage, and continuous variation between the half- and full- bridge is possible. The drawback is additional conduction and switching losses caused by the auxiliary devices.

B. DUTY CYCLE METHODS

An easier way to adjust the equivalent amplitudes of v_{ab}, v_{cd} is to regulate the duty cycles D_1 and D_2 as shown in Fig. 6. v_{ab} can be expressed using Fourier series [39]

$$|\vec{v}_{ab(n)}| = \frac{4\sin(n\pi/2)\sin(D_1 n\pi/2)}{n\pi}V_1, \quad n = 1, 3, 5, \cdots$$

$$(3)$$

where $|\vec{v}_{ab(n)}|$ denotes amplitude of different frequency component. Decreasing D_1 and D_2 can reduce the amplitudes of different frequency components. The duty cycle methods has no limitation on the voltage gain conditions.

Duty cycles D_1, D_2 can be adjusted by extra switching as shown in Fig. 7 (a) [40], [41]. These methods however cause additional switching losses. A more efficient way is to modify
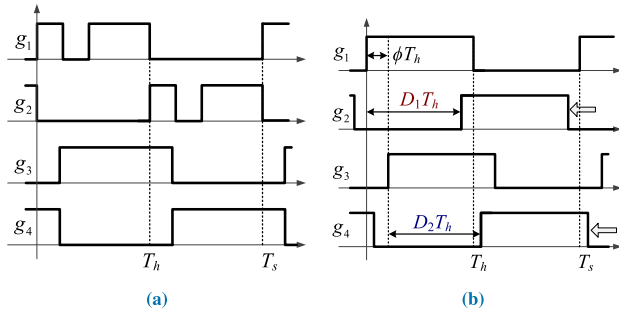
FIGURE 7. Methods to adjust D_1, D_2: (a) extra switching [40], [41] (b) phase shift.

the phase shift angles between legs in both primary and secondary circuits, as shown in Fig. 7 (b), in which g_2 and g_4 are shifted to left compared to conventional SPS modulation. It is possible to shift g_2 and g_4 to different directions to obtain the same D_1 and D_2 [42].

Based on the number of phase shift ratios (D_1, D_2 and ϕ) are manipulated, the phase shift methods to suppress circulating current can be classified as

- Single phase shift (SPS), $D_1 = D_2 = 1$, only ϕ is controlled for output voltage regulation.
- Dual phase shift (DPS), besides ϕ, another degree of freedom is introduced to suppress the circulating current, and there are two possible ways: one is to regulate D_1 or D_2 depending the voltage gain M [43]–[46], and the other is to regulate both D_1 and D_2, but let $D_1 = D_2$ [33], [47]–[49].
- Triple phase shift (TPS), D_1, D_2 and ϕ are controlled independently [39], [50]–[58].

To find the optimal phase shift ratios, the first thing is to select a proper parameter to indicate the amount of circulating current. There is a wide choice in literature, in the time domain analysis, the total power losses [45], [48], reverse power [46], [55], RMS value of inductor current i_L [58], [59] and current stress (I_s in Fig. 9) of i_L [46], [49], [56], [57] have been used. These parameters are all feasible as the increment of circuiting current will increase total power losses, reverse power, RMS value of i_L and current stress. In terms of calculation simplicity, the current stress of i_L is the best choice as all other parameters themselves require intensive calculation in a DAB.

When DAB is modulated using DPS or TPS, the phase shift ratio ϕ cannot reflect the power transfer direction. An example is shown in Fig. 8, where $v_{ab(1)}$ and $v'_{cd(1)}$ are the fundamental frequency components of v_{ab} and v'_{cd} respectively. Although $\phi < 0$, $v_{ab(1)}$ is ahead of $v'_{cd(1)}$ and the output power $P > 0$ (from v_{ab} to v'_{cd}). To avoid this difficulty, the outer phase shift ratio, D_f in Fig. 9, is defined [39], [56]. D_f represents the phase shift between the fundamental components of v_{ab} and v_{cd}, and is expressed as:

$$D_f = \frac{D_2}{2} - \frac{D_1}{2} + \phi \tag{4}$$

Although DPS can reduce the DAB circulating current to some extent, their phase shift variables (D_1, D_2, ϕ) are only

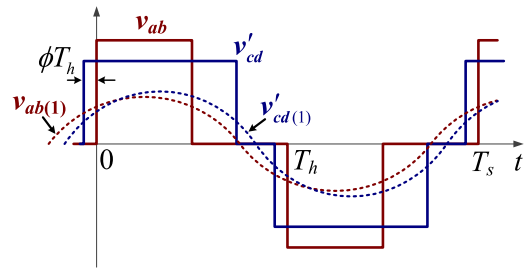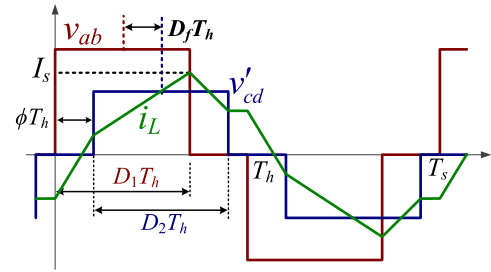**FIGURE 8.** The phase shift angle $\phi < 0$ but output power $P > 0$.

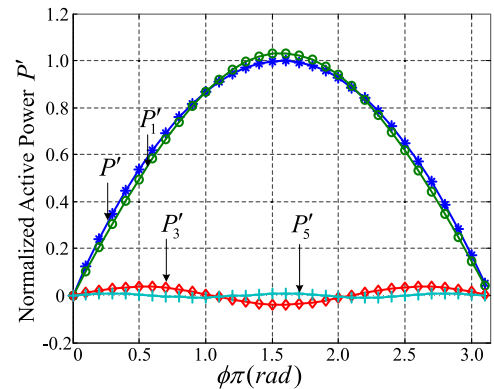**FIGURE 9.** Definition of the outer phase shift ratio D_f [39].

FIGURE 10. Different frequency components of active power of a DAB modulated using SPS: P'_1, P'_3, and P'_5 represent the fundamental, third, and fifth component [39].

locally optimized [56]. This is also the case for preliminary TPS methods including triangular and trapezoidal modulation methods, whose name comes from the inductor current shape [50], [51], [59], [60].

With different operating modes and three degrees of freedom, it is challenging to obtain the global optimal TPS parameters for a DAB. The first way is to approximate square voltages and inductor currents using fundamental components [39], [52], [53]. Fig. 10 shows different frequency components of the active power of a DAB modulated using SPS, and the fundamental component is dominant and can be used approximate the whole power [39]. Based on the fundamental component approximation (FCA), the optimal D_1, D_2, ϕ are obtained by maximizing fundamental power factor [39], minimizing amplitudes of i_L fundamental component [52], or minimizing fundamental reactive power [53]. A typical control block diagram to implement these FCA methods is shown in Fig. 11. The derivation and
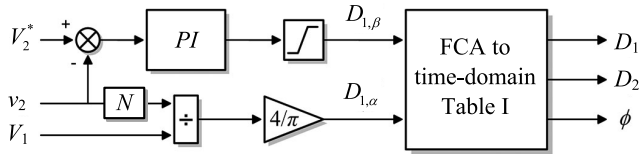
FIGURE 11. Control block diagram to suppress the circulating current based on FCA [52].
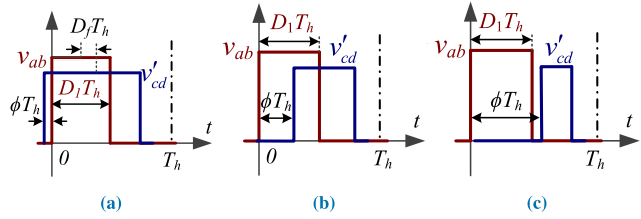

FIGURE 12. DAB operating modes, Mode 1, Mode 2-4, and Modes 5 are differentiated by v'_{cd} rising edge [55], [56], [61]. (a) Mode 1. (b) Mode 2-4. (c) Mode 5.
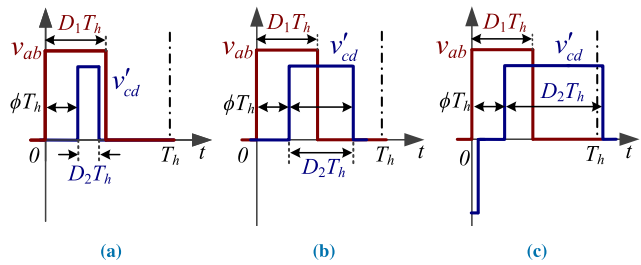

FIGURE 13. DAB operating modes: Mode 2, 3, and 4 are differentiated by v'_{cd} falling edge [55], [56], [61]. (a) Mode 2. (b) Mode 3. (c) Mode 4.

implementation of FCA methods are simple and straight-forward, and can significantly improve the DAB efficiency, nevertheless, FCA of square voltages, inductor current or output power introduce large errors when either D_1 or D_2 is close 0 according to (3) and resultant phase shift ratios are not actually the optimal choice in terms of circulating current minimization.

The other way to derive the optimal phase shift ratios is to analyze DAB in different operating modes in the time domain. This is challenging as a DAB can operate in four different scenarios (forward/backward, buck/boost) and each scenario has different operating modes. It is revealed in [61] that different operating scenarios are equivalent to each other and only one of the scenarios, for instance the forward/buck, requires detailed analysis. In the forward/buck scenario, different operating modes have to be considered as the expressions of the output power are different for each mode. Krismer and Kolar have classified DAB into 12 different modes and pointed out 6 of these modes only increase RMS current of i_L without increasing the power transfer capability [54]. Jain and Ayyanar, Huang *et al.*, and Shao *et al.* have simplified DAB into 5 different operating modes as shown in Figs. 12 and 13, where the different modes are classified based on the relative position between v_{ab} and v'_{cd} [55], [56], [61].

Based on the mode classification in Figs. 12 and 13, Huang *et al.* rigorously derived the global optimal D_1, D_2,
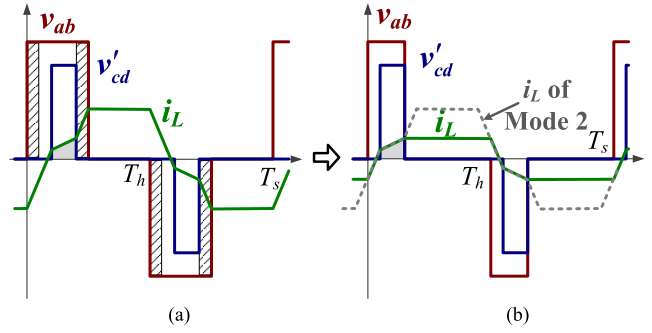

FIGURE 14. Covert operating points of Mode 2 into that of Mode 3 with lower conduction losses [61].

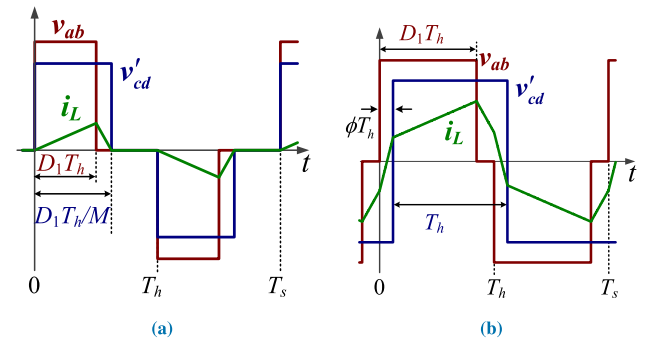**FIGURE 15.** Optimal phase shift ratios (forward/buck scenario) to achieve minimum circulating current [55]–[58]. (a) $0 < P_n \leq M(1-M)/2$. (b) $P_n > M(1-M)/2$.

ϕ using the Karush-Kuhn-Tucker (KKT) method and numerical comparisons [56]. Hou *et al.* also deduced the optimal D_1, D_2, ϕ using the Lagrange multiplier method (LMM), though some of the operating modes are not considered [57]. Huang *et al.* and Hou *et al.* derived the same optimal phase shift ratios minimizing RMS value of inductor current i_L and the derivation process is more complex compared to [56], [57]. The derivation of [56], [57] is simplified in [61], which proves operating points of Mode 1, 2 and 5 can be mapped into that of Mode 3 with lower conduction losses. As an example shown in Fig. 14, shrink of v_{ab} at the rising and falling edges can let the DAB operate from Mode 2 to 3, this conversion does not change the output power, but the RMS value of i_L in Fig. 14 (b) is reduced [61]. This conversion can significantly simplify the derivation process.

The time domain analysis [55]–[58] has found the optimal phase shift ratios to achieve the minimum circulating current, as shown in Table 1 and Fig. 15, where P_n is the normalized output power:

$$P_n = P_o/P_b, P_b = \frac{NV_1V_2}{2fL} \quad (5)$$

However, modulating the DAB using this strategy does not always guarantee the highest efficiency due to the loss of ZVS-on under light load conditions [52], [61]. As shown in Fig. 15 (a), when $P_n \leq M(1-M)/2$, six power devices (two in the primary side and four in the secondary side) turn on when $i_L = 0$ and energy stored in C_{ds} in these devices

TABLE 1. Optimal TPS phase shift ratios in literature ($M < 1, P_o > 0$).

Authors	Phase shift ratios	Optimization target
Zhao *et al.* [39]	$D_1 = 1 - \arccos M, D_2 = 1, \phi$ regulated by v_o	Maximal fundamental active power
Choi *et al.* [52]	$D_1 = \dfrac{1}{\pi} \arcsin(\dfrac{\pi}{4}\sqrt{D_{1,\alpha}^2 + D_{1,\beta}^2}), D_2 = 0.5$ $\phi = \dfrac{1}{2\pi} \arctan(D_{1,\beta}/D_{1,\alpha}),$ *where* $D_{1,\alpha} = \dfrac{4}{\pi}M, D_{1,\beta}$ *is the PI output*	Minimal amplitude of i_L fundamental component
Shi *et al.* [53]	$D_1 = 1 - \dfrac{2}{\pi} \arccos(M/2) \cdot (1 - p*), D_2 = 1$ $\phi = \dfrac{1}{\pi} \arccos \dfrac{M}{2\cos((1-D_1)\pi/2)} + \dfrac{D_1 - D_2}{2}$ *where* $p*$ *is the PI output*	Minimal fundamental reactive power
Jain *et al.* [55]	$\begin{cases} D_1 = \sqrt{\dfrac{2MP_n}{1-M}} & \\ D_2 = \dfrac{D_1}{M}, \phi = 0 & P_n \in [0, \frac{M(1-M)}{2}] \\ D_1 = 1 - (1-M)\sqrt{\dfrac{1-4P_n}{1-2M+2M^2}} & \\ D_2 = 1, \phi = \dfrac{D_1 - M}{2(1-M)} & P_n \in [\frac{M(1-M)}{2}, \frac{1}{4}] \end{cases}$	Minimal i_L peak value (current stress)
Huang *et al.* [56]		
Hou *et al.* [57]		
Tong *et al.* [58]		Minimal i_L RMS value

is dissipated. Actually certain amount of circulating current is required to achieve ZVS-on of power devices [62], and the phase shift ratios derived using FCA [39], [52], [53] have a wider ZVS-on range. Section III will discuss this topic. In addition, the phases shift ratios derived using time domain analysis usually involves various modes and are more complex than that obtained using FCA.

III. ZVS-ON
ZVS-on is more desirable than ZCS of the converters that employ MOSFETs [63]. The most significant switching loss of hard switching MOSFETs are the losses induced by the diode reverse recovery and the energy stored in the MOSFET output capacitance. Turning MOSFET on at zero voltage also eliminates the overvoltage problems associated with parasitic inductance and improves the drive reliability.

This section will firstly give the ZVS-on condition for DAB modulated using SPS, then methods to expand the ZVS-on region are reviewed.

A. ZVS-ON RANGE USING SPS
The ZVS-on range is firstly derived assuming ideal power devices and transformers without considering the device parasitic capacitance and transformer magnetizing inductance. With this assumption, the power devices achieve ZVS-on if the current goes through the anti-parallel diodes at the turn-on point. As shown in Fig. 16 (a) and (b), $i_A < 0$ and $i_B > 0$ should be satisfied to achieve ZVS-on for primary and secondary devices respectively, where v_{ab}, v'_{cd} and i_L are defined in Fig 1.
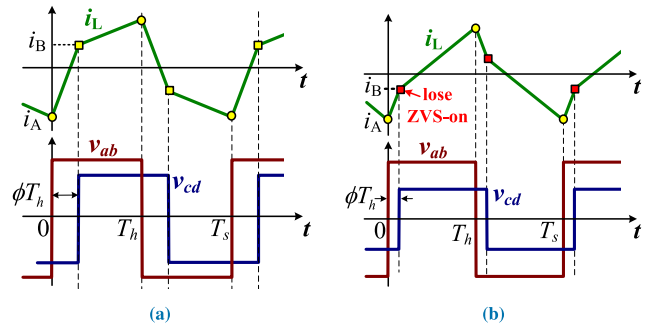
FIGURE 16. (a) All power devices achieve ZVS-on, (b) Secondary devices lose ZVS-on: Yellow-ZVS on, red-loss of ZVS.
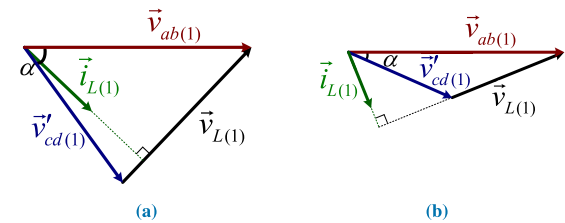
FIGURE 17. Fundamental phasor diagrams of Fig. 16 where the voltage gain $M < 1$. (a) ZVS-on realized. (b) Secondary switches lose ZVS-on.

Compared Fig. 16 (a) and (b), the power devices tend to lose ZVS-on when the output power decreases (ϕ decreases) and the conversion gain M moves away from unity. This phenomenon can be explained using the phasor diagram in Fig. 17, where $\vec{v}_{ab(1)}$, $\vec{v}'_{cd(1)}$ and $\vec{i}_{L(1)}$ in Fig. 17 (a) and (b) are fundamental component phasors of v_{ab}, v'_{cd} and i_L in Fig. 16 (a) and (b) respectively. To maintain ZVS-on for all

FIGURE 18. Fundamental phasor diagrams when $M > 1$. (a) ZVS-on realized. (b) Primary side switches lose ZVS-on.
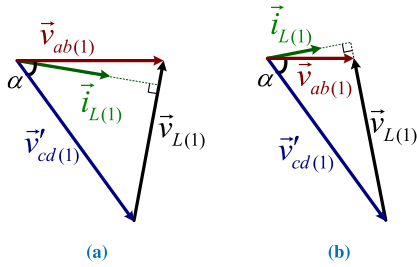
devices, $\vec{i}_{L(1)}$ should lag $\vec{v}_{ab(1)}$ and lead $\vec{v}'_{cd(1)}$ (within the triangle composed by $\vec{v}_{ab(1)}$, $\vec{v}'_{cd(1)}$ and $\vec{v}_{L(1)}$) if the fundamental component approximation is used. Similar analysis can be conducted when $M > 1$ as well, and the corresponding phasor diagram is illustrated in Fig. 18. To let $\vec{i}_{L(1)}$ within the triangle composed by $\vec{v}_{ab(1)}$, $\vec{v}'_{cd(1)}$, we obtain:

$$\begin{cases} \left| \vec{v}'_{cd(1)} \right| > \left| \vec{v}_{ab(1)} \right| \cos\alpha, & when\ M \leq 1 \\ \left| \vec{v}_{ab(1)} \right| > \left| \vec{v}'_{cd(1)} \right| \cos\alpha, & when\ M > 1 \end{cases} \quad (6)$$

where α is angle between $\vec{v}_{ab(1)}$ and $\vec{v}_{cd(1)}$. When SPS modulation is used, $|\vec{v}'_{cd(1)}|/|\vec{v}_{ab(1)}| = v'_{cd}/v_{ab} = M$, and (6) can be written as:

$$\begin{cases} M > \cos\alpha, & when\ M \leq 1 \\ 1/M > \cos\alpha, & when\ M > 1 \end{cases} \quad (7)$$

This equation is the ZVS-on requirements using FCA, and this requirement cannot be met when M is away from unity or α ($\alpha = \phi\pi$) is small (light load condition). From Figs. 17 and 18, we also note that it is always the power devices on lower voltage side tend to lose ZVS-on: when $M < 1$ (Fig. 17), the primary side devices can always realize ZVS-on, but the secondary side devices may lose ZVS-on; while $M > 1$ (Fig. 18), the primary side devices may lose ZVS-on. More precise ZVS-on boundary conditions considering multiple frequency components are derived in [64].

The above conclusions can be validated using the time-domain analysis. Based on the ZVS-on requirements $i_A < 0$, $i_B > 0$, the ZVS-on boundary is plotted in Fig. 19 (a). It is easier to achieve ZVS-on under heavy load and when the gain is close to unity.

In practice, to fully achieve ZVS-on, the energy stored in the leakage inductor should be large enough to fully charge and discharge capacitances of the power switches [65]:

$$\frac{1}{2} L I_{sw}^2 \geq k \frac{1}{2} C_s V_{dc}^2 \quad (8)$$

where k is the number of switching devices, I_{sw} the inductor current at the switching instant, C_s the effective output capacitance of the switching device, and V_{dc} the left or right side dc bus the voltage.

The presence of switch capacitances requires a minimum charge provided by i_L during the dead time interval, thus the ZVS range for DAB is narrower than the ideal condition [66].
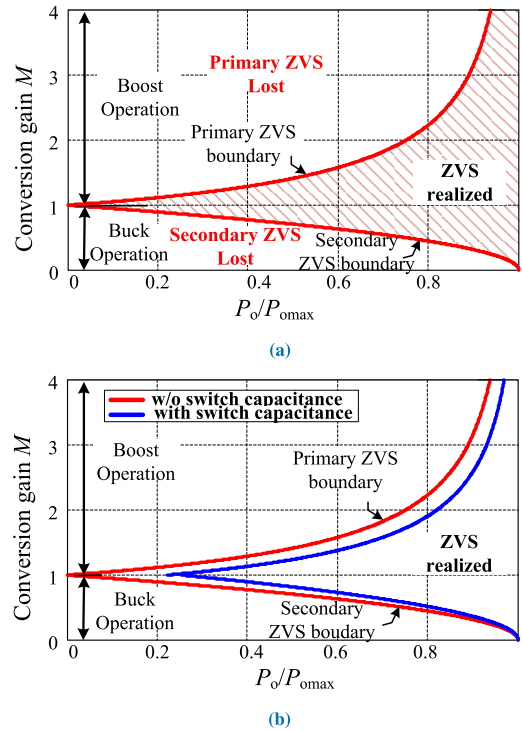

FIGURE 19. ZVS-on range for a DAB modulated using SPS when $P_o > 0$. (a) ZVS-on range in ideal condition. (b) ZVS-on range considering parasitic capacitance.

The calculation is presented in [67], and the result is plotted as blue lines in Fig. 19 (b).

An appropriate dead-time is required to complete the capacitance charging procedure. If the chosen dead-time is too short, a hard-switching or a partial ZVS will result. Assuming the current I_{sw} and the voltage V_{dc} remains constant during the switching transition, the minimum charging time is [65]:

$$t_{dead.min} = \frac{Q}{I_{sw}} = \frac{2V_{dc}C_s}{I_{sw}} \quad (9)$$

where Q is the charge of the switching leg.

B. METHODS TO EXPAND THE ZVS RANGE

Essentially, most of the techniques in Section II to suppress the circulating current can expand the ZVS operating range. The control target of the circulating current suppression is to minimize the angle between $\vec{v}_{ab(1)}$ and $\vec{i}_{L(1)}$, and the angle between $\vec{v}_{cd(1)}$ and $\vec{i}_{L(1)}$, according to (2). This will let $\vec{i}_{L(1)}$ inside the triangle composed by $\vec{v}_{ab(1)}$, $\vec{v}_{cd(1)}$ and $\vec{v}_{L(1)}$.

The duty cycle methods that adjust D_1 and D_2 to let the equivalent gain M close to unity, can assist the ZVS-on according to (7). Nevertheless, the TPS methods with minimum circulating current [55]–[58] cannot achieve ZVS-on in the whole operating range as explained in end of Section II. Actually, certain circulating current is required to charge and discharge the capacitance of power devices and the TPS methods derived using FCA [39], [52], [53] have a wider ZVS-on operating range.
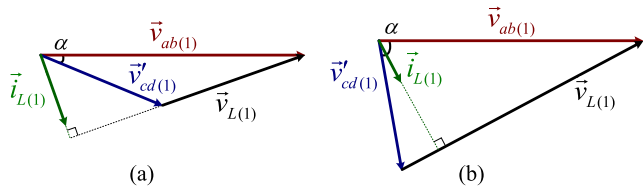
FIGURE 20. Phasor diagram of a DAB under the same output power: (a) low switching frequency and ZVS-on lost (b) high switching frequency, ZVS-on realized [65], [68].
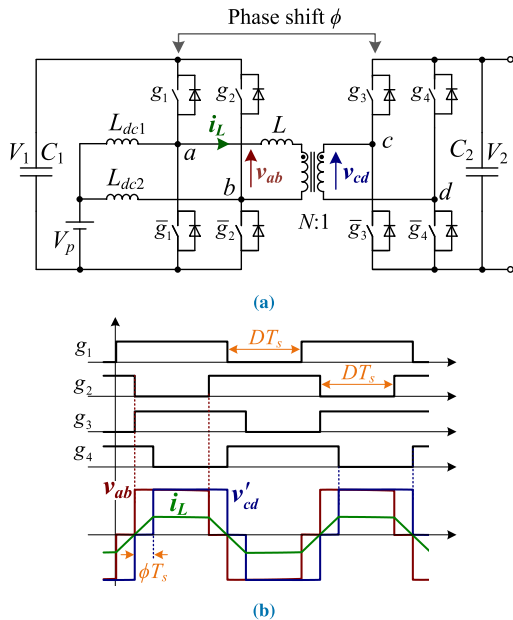

FIGURE 22. Expand ZVS-on range by adjusting inductor *L* under different load conditions [75], [76].

FIGURE 21. (a) Typical CF-DAB circuit (b) its key waveforms [71], [72].

FIGURE 23. Expand ZVS-on range using additional controlled voltage source: (a) simplified circuit, (b) phasor diagram [78]–[80].

Frequency modulation in Fig. 20 can expand the ZVS range [65], [68]. Since the DAB output power $P_o \propto 1/f$, under light load conditions, a high f can maintain rather a large phase shift ratio α ($\alpha = \phi\pi$) for a given power, such that the ZVS operation requirements (7) can be met. In [65], the frequency f and phase shift angle ϕ are chosen such that, when the power devices at the lower voltage side switching, the inductor current i_L is equal to a predefined value and able to charge/discharge the power device capacitances. Of course, there is limit on the switching frequency range to avoid transformer saturation.

A number of hardware methods have been proposed to expand the ZVS-on operating range. One of the most important innovation is the current fed DAB (CF-DAB) converter. Firstly proposed by F. Z. Peng *et. al*. [69], CF-DAB gains growing recognition in energy storage and photovoltaic (PV) applications [70], [71]. A CF-DAB integrates buck/boost converters and a DAB (Fig. 21 (a)), and can regulate V_1 on the primary side capacitor C_1 by adjusting D and maintain a close-to-unity voltage gain under different load conditions as shown in Fig. 21 (b), and the loss of ZVS and circulating current problems can be naturally solved [71]–[73]. Another desirable feature of a CF-DAB is the low current ripple. These features make CF-DAB a good choice in ESS applications.
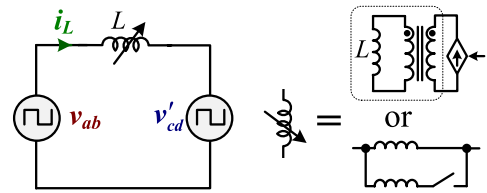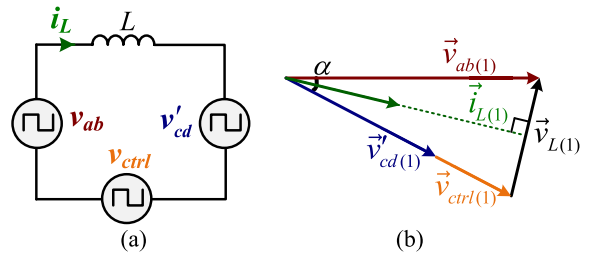
A CF-DAB is easy to interleave more phases to reduce size of input dc inductors and dc link capacitors [74].

Adjusting the inductor L depending on load conditions can expand the ZVS operating range, as shown in Fig. 22 [75], [76]. Since the DAB output power $P_o \propto 1/L$, under light load conditions, a high inductance is inserted to maintain rather a large phase shift ratio ϕ, such that the ZVS operation requirements (7) can be met. The inductance of L can be adjusted by applying a bias current to L [75] or by paralleling a switch controlled inductor [76], [77], as shown in Fig. 22.

The ZVS operation range can also be expanded by adding another controlled voltage source, as shown in Fig. 23 [78]–[81]. The operating principle is illustrated using the phasor diagram in Fig. 23 (b). v_{ctrl} is adjusted according to voltage gain and load conditions, such that $\vec{i}_{L(1)}$ is inside the triangle composed by $\vec{v}_{ab(1)}$, $\vec{v}_{cd(1)}$ and $\vec{v}_{L(1)}$, then all the power devices can achieve ZVS-on according to Figs. 17, 18 and (7). v_{ctrl} can be implemented by inserting an auxiliary circuit consisting of a transformer and a H-bridge [79], [80] as shown in Fig. 24, where the auxiliary H-bridge is in parallel with the DAB bridge circuit. The auxiliary H-bridge can also be in series of the DAB bridge circuit [81].

Paralleling a switch controlled inductor to the DAB transformer can manipulate the current at the switching instance and hence expands the ZVS operation range, as shown in Fig. 25 [82]. The operating principle is illustrated using the phasor diagram in Fig. 25 (b). By switching S_a according to load conditions, the amplitude of $\vec{i}_a$ is regulated to let $\vec{i}_{Ls(1)}$ within the triangle composed by $\vec{v}_{ab(1)}$, $\vec{v}_{cd(1)}$ and $\vec{v}_{L(1)}$. A similar circuit is presented in [83]. Decreasing the transformer magnetizing inductance, by increasing the magnetic core air gap, can also expand the ZVS range [84]. This will however increase conduction losses in power devices and the transformer due to the increased i_L.
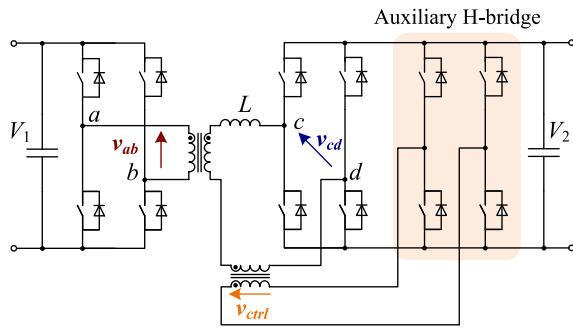
FIGURE 24. Implementation of v_{ctrl} in Fig. 23 using an auxiliary circuit [79], [80].
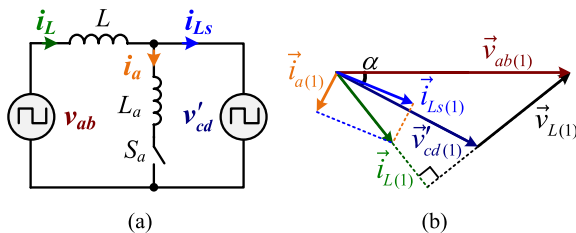

FIGURE 25. Expand ZVS-on range by paralleling a switch controlled inductor: (a) simplified circuit, (b) phasor diagram [82].

IV. CONCLUSION

Unmatched voltage gain and light load are the primary reasons of the large circulating current and loss of ZVS, and comprehensive explanations using fundamental phasor diagrams are presented. Various hardware and control methods have been proposed in literature to suppress the circulating current and expand the ZVS-on range, and the core idea of these methods is often to let the equivalent voltage gain close to unity.

Hardware methods often require additional power semiconductor devices, adding additional cost and losses and its expected improvements are often not as good as the control methods. However, *current fed DAB* is a very promising circuit that can maintain a close-to-unity voltage gain under different load conditions, and no additional power devices are required.

Varying switching frequency or inductance can increase phase shift angle under light load to extend ZVS range and can decrease phase shift angle at heavy load to reduce circulating energy and maintain ZVS-on. Of course, there is limit on the switching frequency range to avoid transformer saturation. In addition, in each switching frequency, it is possible to adjust duty cycle to suppress the circulating current.

Among the duty cycle methods, the time domain analysis has found the optimal phase shift ratios to achieve the minimum circulating current. This strategy can be useful in high power applications with high current and low switching frequency such as solid state transformers. In high frequency applications, however, this strategy does not always guarantee the highest efficiency due to the loss of ZVS-on under light load conditions. Certain amount of circulating current

is required to achieve ZVS-on of power devices, this is the reason why the phase shift ratios derived using FCA have a wider ZVS-on range. It is beneficial to optimize the circulating current and ZVS-on issues as a whole and such attempts have been made by [51], [62]. Four degrees of freedom, the three phase shift ratios and the switching frequency, can be considered during these optimizations [62].

REFERENCES

[1] B. Dudley, "BP statistical review of world energy 2017," British Petroleum Co., London, U.K., 2017.

[2] N. Hatziargyriou, *Microgrids: Architectures and Control*. Hoboken, NJ, USA: Wiley, 2014. [Online]. Available: https://books.google.co.jp/books?id=ywxzAgAAQBAJ

[3] M. Faisal, M. A. Hannan, P. J. Ker, A. Hussain, M. Mansur, and F. Blaabjerg, "Review of energy storage system technologies in microgrid applications: Issues and challenges," *IEEE Access*, vol. 6, pp. 35143–35164, 2018.

[4] D. Boroyevich, I. Cvetković, D. Dong, R. Burgos, F. Wang, and F. Lee, "Future electronic power distribution systems a contemplative view," in *Proc. 12th Int. Conf. Optim. Elect. Electron. Equip.*, May 2010, pp. 1369–1380.

[5] W. Medjroubi, U. P. Müller, M. Scharf, C. Matke, and D. Kleinhans, "Open data in power grid modelling: New approaches towards transparent grid models," *Energy Rep.*, vol. 3, pp. 14–21, Nov. 2017. [Online]. Available: http://www.sciencedirect.com/science/article/pii/S2352484716300877

[6] A. Q. Huang, M. L. Crow, G. T. Heydt, J. P. Zheng, and S. J. Dale, "The future renewable electric energy delivery and management (FREEDM) system: The energy Internet," *Proc. IEEE*, vol. 99, no. 1, pp. 133–148, Jan. 2011.

[7] B. Zhao, S. Qiang, W. Liu, and Y. Sun, "Overview of dual-active-bridge isolated bidirectional DC-DC converter for high-frequency-link power-conversion system," *IEEE Trans. Power Electron.*, vol. 29, no. 8, pp. 4091–4106, Aug. 2014.

[8] R. W. De Doncker, D. M. Divan, and M. H. Kheraluwala, "A three-phase soft-switched high power density DC/DC converter for high power applications," in *Proc. Conf. Rec. IEEE Ind. Appl. Soc. Annu. Meeting*, vol. 1, Oct. 1988, pp. 796–805.

[9] R. W. A. A. De Doncker, D. M. Divan, and M. H. Kheraluwala, "A three-phase soft-switched high-power-density DC/DC converter for high-power applications," *IEEE Trans. Ind. Appl.*, vol. 27, no. 1, pp. 63–73, Jan. 1991.

[10] A. Q. Huang, "Medium-voltage solid-state transformer: Technology for a smarter and resilient grid," *IEEE Ind. Electron. Mag.*, vol. 10, no. 3, pp. 29–42, Sep. 2016.

[11] J. Shi *et al.*, "Research on voltage and power balance control for cascaded modular solid-state transformer," *IEEE Trans. Power Electron.*, vol. 26, no. 4, pp. 1154–1166, Apr. 2011.

[12] S. Inoue and H. Akagi, "A bidirectional isolated DC–DC converter as a core circuit of the next-generation medium-voltage power conversion system," *IEEE Trans. Power Electron.*, vol. 22, no. 2, pp. 535–542, Mar. 2007.

[13] D. Rothmund, G. Ortiz, T. Guillod, and J. W. Kolar, "10 kV SiC-based isolated DC–DC converter for medium voltage-connected solid-state transformers," in *Proc. IEEE Appl. Power Electron. Conf. Expo. (APEC)*, Mar. 2015, pp. 1096–1103.

[14] S. Falcones, R. Ayyanar, and X. Mao, "A DC–DC multiport-converter-based solid-state transformer integrating distributed generation and storage," *IEEE Trans. Power Electron.*, vol. 28, no. 5, pp. 2192–2203, May 2013.

[15] S. Shao, M. Jiang, J. Zhang, and X. Wu, "A capacitor voltage balancing method for a modular multilevel DC transformer for DC distribution system," *IEEE Trans. Power Electron.*, vol. 33, no. 4, pp. 3002–3011, Apr. 2018.

[16] D. Jovcic and H. Zhang, "Dual channel control with DC fault ride through for MMC-based, isolated DC/DC converter," *IEEE Trans. Power Del.*, vol. 32, no. 3, pp. 1574–1582, Jun. 2017.

[17] B. Zhao, Q. Song, J. Li, and W. Liu, "A modular multilevel DC-link front-to-front DC solid-state transformer based on high-frequency dual active phase shift for HVDC grid integration," *IEEE Trans. Ind. Electron.*, vol. 64, no. 11, pp. 8919–8927, Nov. 2017.

[18] D. Dujic *et al.*, "Power electronic traction transformer-low voltage prototype," *IEEE Trans. Power Electron.*, vol. 28, no. 12, pp. 5522–5534, Dec. 2013.

[19] C. Zhao *et al.*, "Power electronic traction transformer—Medium voltage prototype," *IEEE Trans. Ind. Electron.*, vol. 61, no. 7, pp. 3257–3268, Jul. 2014.

[20] B. Thomas, M. Akos, and D. Dujic, "Power electronic traction transformer: Efficiency improvements under light-load conditions," *IEEE Trans. Power Electron.*, vol. 29, no. 8, pp. 3971–3981, Aug. 2014.

[21] J. Liu, J. Yang, J. Zhang, Z. Nan, and Q. Zheng, "Voltage balance control based on dual active bridge DC/DC converters in a power electronic traction transformer," *IEEE Trans. Power Electron.*, vol. 33, no. 2, pp. 1696–1714, Feb. 2018.

[22] L. Xue, Z. Shen, D. Boroyevich, P. Mattavelli, and D. Diaz, "Dual active bridge-based battery charger for plug-in hybrid electric vehicle with charging current containing low frequency ripple," *IEEE Trans. Power Electron.*, vol. 30, no. 12, pp. 7299–7307, Dec. 2015.

[23] P. He and A. Khaligh, "Comprehensive analyses and comparison of 1 kW isolated DC–DC converters for bidirectional EV charging systems," *IEEE Trans. Transport. Electrific.*, vol. 3, no. 1, pp. 147–156, Mar. 2017.

[24] R. Hou and A. Emadi, "A primary full-integrated active filter auxiliary power module in electrified vehicles with single-phase onboard chargers," *IEEE Trans. Power Electron.*, vol. 32, no. 11, pp. 8393–8405, Nov. 2017.

[25] J. Lu *et al.*, "A modular-designed three-phase high-efficiency high-power-density ev battery charger using dual/triple-phase-shift control," *IEEE Trans. Power Electron.*, vol. 33, no. 9, pp. 8091–8100, Sep. 2018.

[26] S. Inoue and H. Akagi, "A bidirectional DC–DC converter for an energy storage system with galvanic isolation," *IEEE Trans. Power Electron.*, vol. 22, no. 6, pp. 2299–2306, Nov. 2007.

[27] Z. Zhang, Y.-Y. Cai, Y. Zhang, D.-J. Gu, and Y.-F. Liu, "A distributed architecture based on microbank modules with self-reconfiguration control to improve the energy efficiency in the battery energy storage system," *IEEE Trans. Power Electron.*, vol. 31, no. 1, pp. 304–317, Jan. 2016.

[28] C. Gammeter, F. Krismer, and J. W. Kolar, "Comprehensive conceptualization, design, and experimental verification of a weight-optimized all-SiC 2 kV/700 V DAB for an airborne wind turbine," *IEEE J. Emerg. Sel. Topics Power Electron.*, vol. 4, no. 2, pp. 638–656, Jun. 2016.

[29] Y. W. Cho, W. J. Cha, J. M. Kwon, and B. H. Kwon, "High-efficiency bidirectional DAB inverter using a novel hybrid modulation for stand-alone power generating system with low input voltage," *IEEE Trans. Power Electron.*, vol. 31, no. 6, pp. 4138–4147, Jun. 2016.

[30] H. Y. Kanaan, M. Caron, and K. Al-Haddad, "Design and implementation of a two-stage grid-connected high efficiency power load emulator," *IEEE Trans. Power Electron.*, vol. 29, no. 8, pp. 3997–4006, Aug. 2014.

[31] A. S. Babokany, M. Jabbari, G. Shahgholian, and M. Mahdavian, "A review of bidirectional dual active bridge converter," in *Proc. 9th Int. Conf. Elect. Eng./Electron., Comput., Telecommun. Inf. Technol. (ECTI-CON)*, May 2012, pp. 1–4.

[32] C. Mi, H. Bai, C. Wang, and S. Gargies, "Operation, design and control of dual H-bridge-based isolated bidirectional DC-DC converter," *IET Power Electron.*, vol. 1, no. 4, pp. 507–517, Dec. 2008.

[33] H. Bai and C. Mi, "Eliminate reactive power and increase system efficiency of isolated bidirectional dual-active-bridge DC-DC converters using novel dual-phase-shift control," *IEEE Trans. Power Electron.*, vol. 23, no. 6, pp. 2905–2914, Nov. 2008.

[34] J. Zhang, F. Zhang, X. Xie, D. Jiao, and Z. Qian, "A novel ZVS DC/DC converter for high power applications," *IEEE Trans. Power Electron.*, vol. 19, no. 2, pp. 420–429, Mar. 2004.

[35] D. Sha, J. Zhang, and Y. Xu, "Improved boundary operation for voltage-fed semi-DAB with ZVS achievement and nonactive power reduction," *IEEE Trans. Ind. Electron.*, vol. 64, no. 8, pp. 6179–6189, Aug. 2017.

[36] V. Karthikeyan and R. Gupta, "FRS-DAB converter for elimination of circulation power flow at input and output ends," *IEEE Trans. Ind. Electron.*, vol. 65, no. 3, pp. 2135–2144, Mar. 2018.

[37] Z. Qin, Y. Shen, P. C. Loh, H. Wang, and F. Blaabjerg, "A dual active bridge converter with an extended high-efficiency range by DC blocking capacitor voltage control," *IEEE Trans. Power Electron.*, vol. 33, no. 7, pp. 5949–5966, Jul. 2018.

[38] G. Xu, D. Sha, Y. Xu, and X. Liao, "Hybrid-bridge-based DAB converter with voltage match control for wide voltage conversion gain application," *IEEE Trans. Power Electron.*, vol. 33, no. 2, pp. 1378–1388, Feb. 2018.

[39] B. Zhao, Q. Song, W. Liu, G. Liu, and Y. Zhao, "Universal high-frequency-link characterization and practical fundamental-optimal strategy for dual-active-bridge DC-DC converter under PWM plus phase-shift control," *IEEE Trans. Power Electron.*, vol. 30, no. 12, pp. 6488–6494, Dec. 2015.

[40] T. Hirose, M. Takasaki, and Y. Ishizuka, "A power efficiency improvement technique for a bidirectional dual active bridge DC–DC converter at light load," *IEEE Trans. Ind. Appl.*, vol. 50, no. 6, pp. 4047–4055, Nov. 2014.

[41] H. Wang, K. Yan, Z. Ling, and J. Gan, "Switching strategy for isolated dual-active-bridge converter," *IET Power Electron.*, vol. 10, no. 1, pp. 29–37, 2017.

[42] X. Liu *et al.*, "Novel dual-phase-shift control with bidirectional inner phase shifts for a dual-active-bridge converter having low surge current and stable power control," *IEEE Trans. Power Electron.*, vol. 32, no. 5, pp. 4095–4106, May 2017.

[43] K. Vangen, T. Melaa, S. Bergsmark, and R. Nilsen, "Efficient high-frequency soft-switched power converter with signal processor control," in *Proc. 13th Int. Telecommun. Energy Conf. (INTELEC)*, Nov. 1991, pp. 631–639.

[44] K. Vangen, T. Melaa, and A. K. Adnanes, "Soft-switched high-frequency, high power DC/AC converter with IGBT," in *Proc. Rec. 23rd Annu. IEEE Power Electron. Spec. Conf. (PESC)*, vol. 1, Jun. 1992, pp. 26–33.

[45] G. G. Oggier, G. O. García, and A. Oliva, "Switching control strategy to minimize dual active bridge converter losses," *IEEE Trans. Power Electron.*, vol. 24, no. 7, pp. 1826–1838, Jul. 2009.

[46] B. Zhao, Q. Yu, and W. Sun, "Extended-phase-shift control of isolated bidirectional DC-DC converter for power distribution in microgrid," *IEEE Trans. Power Electron.*, vol. 27, no. 11, pp. 4667–4680, Nov. 2012.

[47] B. Zhao, Q. Song, and W. Liu, "Power characterization of isolated bidirectional dual-active-bridge DC-DC converter with dual-phase-shift control," *IEEE Trans. Power Electron.*, vol. 27, no. 9, pp. 4172–4176, Sep. 2012.

[48] B. Zhao, Q. Song, and W. Liu, "Efficiency characterization and optimization of isolated bidirectional DC-DC converter based on dual-phase-shift control for DC distribution application," *IEEE Trans. Power Electron.*, vol. 28, no. 4, pp. 1711–1727, Apr. 2013.

[49] B. Zhao, Q. Song, W. Liu, and W. Sun, "Current-stress-optimized switching strategy of isolated bidirectional DC–DC converter with dual-phase-shift control," *IEEE Trans. Ind. Electron.*, vol. 60, no. 10, pp. 4458–4467, Oct. 2013.

[50] N. Schibli, "Symmetrical multilevel converters with two quadrant DC-DC feeding," Ph.D. dissertation, EPFL, Lausanne, Switzerland, 2000.

[51] F. Krismer, "Modeling and optimization of bidirectional dual active bridge DC-DC converter topologies," Ph.D. dissertation, ETH Zürich, Zürich, Switzerland, 2010.

[52] W. Choi, K.-M. Rho, and B.-H. Cho, "Fundamental duty modulation of dual-active-bridge converter for wide-range operation," *IEEE Trans. Power Electron.*, vol. 31, no. 6, pp. 4048–4064, Jun. 2016.

[53] H. Shi, H. Wen, J. Chen, Y. Hu, L. Jiang, and G. Chen, "Minimum-reactive-power scheme of dual-active-bridge DC–DC converter with three-level modulated phase-shift control," *IEEE Trans. Ind. Appl.*, vol. 53, no. 6, pp. 5573–5586, Nov. 2017.

[54] F. Krismer and J. W. Kolar, "Closed form solution for minimum conduction loss modulation of DAB converters," *IEEE Trans. Power Electron.*, vol. 27, no. 1, pp. 174–188, Jan. 2012.

[55] A. K. Jain and R. Ayyanar, "PWM control of dual active bridge: Comprehensive analysis and experimental verification," *IEEE Trans. Power Electron.*, vol. 26, no. 4, pp. 1215–1227, Apr. 2011.

[56] J. Huang, Y. Wang, Z. Li, and W. Lei, "Unified triple-phase-shift control to minimize current stress and achieve full soft-switching of isolated bidirectional DC-DC converter," *IEEE Trans. Ind. Electron.*, vol. 63, no. 7, pp. 4169–4179, Jul. 2016.

[57] N. Hou, W. Song, and M. Wu, "Minimum-current-stress scheme of dual active bridge DC–DC converter with unified phase-shift control," *IEEE Trans. Power Electron.*, vol. 31, no. 12, pp. 8552–8561, Dec. 2016.

[58] A. Tong, L. Hang, G. Li, X. Jiang, and S. Gao, "Modeling and analysis of a dual-active-bridge-isolated bidirectional DC/DC converter to minimize RMS current with whole operating range," *IEEE Trans. Power Electron.*, vol. 33, no. 6, pp. 5302–5316, Jun. 2018.

[59] G. Xu, D. Sha, J. Zhang, and X. Liao, "Unified boundary trapezoidal modulation control utilizing fixed duty cycle compensation and magnetizing current design for dual active bridge DC–DC converter," *IEEE Trans. Power Electron.*, vol. 32, no. 3, pp. 2243–2252, Mar. 2017.

[60] H. Zhou and A. M. Khambadkone, "Hybrid modulation for dual-active-bridge bidirectional converter with extended power range for ultracapacitor application," *IEEE Trans. Ind. Appl.*, vol. 45, no. 4, pp. 1434–1442, Jul./Aug. 2009.

[61] S. Shao, M. Jiang, W. Ye, Y. Li, J. Zhang, and K. Sheng, "Optimal phase shift control to minimize reactive power for a dual active bridge DC-DC converter," *IEEE Trans. Power Electron.*, to be published.

[62] M. Yaqoob, K. H. Loo, and Y. M. Lai, "A four-degrees-of-freedom modulation strategy for dual-active-bridge series-resonant converter designed for total loss minimization," *IEEE Trans. Power Electron.*, vol. 34, no. 2, pp. 1065–1081, Feb. 2019.

[63] R. W. Erickson and D. Maksimovic, *Fundamentals of Power Electronics*. New York, NY, USA: Springer, 2007.

[64] J. Riedel, D. G. Holmes, B. P. McGrath, and C. Teixeira, "ZVS soft switching boundaries for dual active bridge DC–DC converters using frequency domain analysis," *IEEE Trans. Power Electron.*, vol. 32, no. 4, pp. 3166–3179, Apr. 2017.

[65] J. Hiltunen, V. Väisänen, R. Juntunen, and P. Silventoinen, "Variable-frequency phase shift modulation of a dual active bridge converter," *IEEE Trans. Power Electron.*, vol. 30, no. 12, pp. 7138–7148, Dec. 2015.

[66] F. Krismer and J. W. Kolar, "Efficiency-optimized high-current dual active bridge converter for automotive applications," *IEEE Trans. Ind. Electron.*, vol. 59, no. 7, pp. 2745–2760, Jul. 2012.

[67] M. N. Kheraluwala, R. W. Gascoigne, D. M. Divan, and E. D. Baumann, "Performance characterization of a high-power dual active bridge DC-to-DC converter," *IEEE Trans. Ind. Appl.*, vol. 28, no. 6, pp. 1294–1301, Nov./Dec. 1992.

[68] J. Lu *et al.*, "Applying variable-switching-frequency variable-phase-shift control and E-mode GaN HEMTs to an indirect matrix converter-based EV battery charger," *IEEE Trans. Transport. Electric.*, vol. 3, no. 3, pp. 554–564, Sep. 2017.

[69] F. Z. Peng, H. Li, G.-J. Su, and J. S. Lawler, "A new ZVS bidirectional DC-DC converter for fuel cell and battery application," *IEEE Trans. Power Electron.*, vol. 19, no. 1, pp. 54–65, Jan. 2004.

[70] Y. Shi, R. Li, Y. Xue, and H. Li, "High-frequency-link-based grid-tied PV system with small DC-link capacitor and low-frequency ripple-free maximum power point tracking," *IEEE Trans. Power Electron.*, vol. 31, no. 1, pp. 328–339, Jan. 2016.

[71] Y. Shi, R. Li, Y. Xue, and H. Li, "Optimized operation of current-fed dual active bridge DC-DC converter for PV applications," *IEEE Trans. Ind. Electron.*, vol. 62, no. 11, pp. 6986–6995, Nov. 2015.

[72] Z. Guo, K. Sun, T.-F. Wu, and C. Li, "An improved modulation scheme of current-fed bidirectional DC–DC converters for loss reduction," *IEEE Trans. Power Electron.*, vol. 33, no. 5, pp. 4441–4457, May 2018.

[73] D. Sha, X. Wang, and D. Chen, "High-efficiency current-fed dual active bridge DC–DC converter with ZVS achievement throughout full range of load using optimized switching patterns," *IEEE Trans. Power Electron.*, vol. 33, no. 2, pp. 1347–1357, Feb. 2018.

[74] Z. Wang and H. Li, "A soft switching three-phase current-fed bidirectional DC–DC converter with high efficiency over a wide input voltage range," *IEEE Trans. Power Electron.*, vol. 27, no. 2, pp. 669–684, Feb. 2012.

[75] H. Fan and H. Li, "High-frequency transformer isolated bidirectional DC–DC converter modules with high efficiency over wide load range for 20 kVA solid-state transformer," *IEEE Trans. Power Electron.*, vol. 26, no. 12, pp. 3599–3608, Dec. 2011.

[76] G. Guidi, M. Pavlovsky, A. Kawamura, T. Imakubo, and Y. Sasaki, "Improvement of light load efficiency of dual active bridge DC–DC converter by using dual leakage transformer and variable frequency," in *Proc. IEEE Energy Convers. Congr. Expo.*, Sep. 2010, pp. 830–837.

[77] A. Rodriguez, A. Vazquez, D. G. Lamar, M. M. Hernando, and J. Sebastian, "Different purpose design strategies and techniques to improve the performance of a dual active bridge with phase-shift control," *IEEE Trans. Power Electron.*, vol. 30, no. 2, pp. 790–804, Feb. 2015.

[78] G. Xu, D. Sha, Y. Xu, and X. Liao, "Dual-transformer-based DAB converter with wide ZVS range for wide voltage conversion gain application," *IEEE Trans. Ind. Electron.*, vol. 65, no. 4, pp. 3306–3316, Apr. 2018.

[79] A. K. Tripathi *et al.*, "A novel ZVS range enhancement technique of a high-voltage dual active bridge converter using series injection," *IEEE Trans. Power Electron.*, vol. 32, no. 6, pp. 4231–4245, Jun. 2017.

[80] A. Tripathi, K. Mainali, and S. Bhattacharya, "A series compensation enabled ZVS range enhancement of a dual active bridge converter for wide range load conditions," in *Proc. IEEE Energy Convers. Congr. Expo. (ECCE)*, Sep. 2014, pp. 5384–5391.

[81] R. Abramson, S. J. Gunter, D. Otten, K. K. Afridi, and D. J. Perreault, "Design and evaluation of a reconfigurable stacked active bridge DC–DC converter for efficient wide load range operation," *IEEE Trans. Power Electron.*, vol. 33, no. 12, pp. 10428–10448, Dec. 2018.

[82] M. Yaqoob, K. H. Loo, and Y. M. Lai, "Extension of soft-switching region of dual-active-bridge converter by a tunable resonant tank," *IEEE Trans. Power Electron.*, vol. 32, no. 12, pp. 9093–9104, Dec. 2017.

[83] Y. Shen, X. Sun, W. Li, X. Wu, and B. Wang, "A modified dual active bridge converter with hybrid phase-shift control for wide input voltage range," *IEEE Trans. Power Electron.*, vol. 31, no. 10, pp. 6884–6900, Oct. 2016.

[84] J. Riedel, D. G. Holmes, B. McGrath, and C. Teixeira, "Maintaining continuous ZVS operation of a dual active bridge by reduced coupling transformers," *IEEE Trans. Ind. Electron.*, vol. 65, no. 12, pp. 9438–9448, Dec. 2018.

SHUAI SHAO (M'17) received the B.S. degree from Zhejiang University, China, in 2010, and the Ph.D. degree in electrical engineering from the University of Nottingham, U.K., in 2015.

In 2015, he joined the College of Electrical Engineering, Zhejiang University, as a Lecturer. His research interests include solid-state transformers, bidirectional dc–dc converters, and fault detection in power converters.

HUI CHEN was born in Zhejiang, China, in 1988. She received the B.S. and Ph.D. degrees in electrical engineering from Zhejiang University, Hangzhou, China, in 2010 and 2015, respectively.

She is currently with the Zhejiang University City College, Hangzhou. Her current research interests include high-efficiency dc–dc converters and topology research.

XINKE WU (M'09) received the B.S. and M.S. degrees in electrical engineering from the Harbin Institute of Technology, Harbin, China, in 2000 and 2002, respectively, and the Ph.D. degree in electrical engineering from Zhejiang University, Hangzhou, China, in 2006.

From 2007 to 2009, he was a Postdoctoral Fellow with the National Engineering Research Center (NERC) for Applied Power Electronics, Zhejiang University. From 2009 to 2010, he was an Assistant Research Fellow with the Institute of Power Electronics, Zhejiang University, where he was an Associate Professor, from 2011 to 2015. From 2011 to 2012, he was a Visiting Scholar with the Center of Power Electronics System (CPES), Virginia Tech. Since 2009, he has been with the Institute of Power Electronics, Zhejiang University. He is currently a Professor. His research interests include high frequency, high power density and high-efficiency power conversion, power electronics system integration, and high-efficiency LED driving technology. He received Young Scholar Award from Zhejiang University in 2012, Young Scholar Award from NSF of China in 2015, and Young Scholar Award from CPSS of China, 2017.

JUNMING ZHANG (M'10–SM'13) received the B.S., M.S., and Ph.D. degrees in electrical engineering from Zhejiang University, Hangzhou, China, in 1996, 2000, and 2004, respectively.

From 2010 to 2011, he was a Visiting Scholar with the Department of Electrical and Computer Engineering, Michigan State University, East Lansing. He is currently a Professor with the College of Electrical Engineering, Zhejiang University. His research interests include power electronics system integrations, power management, and high-efficiency converters.

Dr. Zhang is an Associate Editor of the IEEE Transactions on Industry Applications and the *CPSS Transactions Power Electronics and Application*.

KUANG SHENG (M'99–SM'08) received the B.Sc. degree from Zhejiang University, Hangzhou, China, in 1995, and the Ph.D. degree from Heriot-Watt University, Edinburgh, U.K., in 1999.

He is currently a Professor with Zhejiang University. His current research interests include all aspects of power semiconductor devices and ICs on SiC and Si.

• • •